Mathematical Modeling of Fluid Flow in a Water Physical Model of an Aluminum Degassing Ladle Equipped with an Impeller-Injector

EUDOXIO RAMOS GÓMEZ, ROBERTO ZENIT, CARLOS GONZÁLEZ RIVERA, GERARDO TRÁPAGA, and MARCO A. RAMÍREZ-ARGÁEZ

In this work, a 3D numerical simulation using a Euler–Euler-based model implemented into a commercial CFD code was used to simulate fluid flow and turbulence structure in a water physical model of an aluminum ladle equipped with an impeller for degassing treatment. The effect of critical process parameters such as rotor speed, gas flow rate, and the point of gas injection (conventional injection through the shaft *vs* a novel injection through the bottom of the ladle) on the fluid flow and vortex formation was analyzed with this model. The commercial CFD code PHOENICS 3.4 was used to solve all conservation equations governing the process for this two-phase fluid flow system. The mathematical model was reasonably well validated against experimentally measured liquid velocity and vortex sizes in a water physical model built specifically for this investigation. From the results, it was concluded that the angular speed of the impeller is the most important parameter in promoting better stirred baths and creating smaller and better distributed bubbles in the liquid. The pumping effect of the impeller is increased as the impeller rotation speed increases. Gas flow rate is detrimental to bath stirring and diminishes the pumping effect of the impeller. Finally, although the injection point was the least significant variable, it was found that the "novel" injection improves stirring in the ladle.

I. INTRODUCTION

ALUMINUM castings for automotive applications are commonly produced by foundry processes which include a refining stage where dissolved hydrogen and other impurities are removed from the melt through the injection of inert gases. This refinement operation determines to a great extent the quality of the product, and it must be optimized with the final objective of producing high quality castings as in the case of automobile and aerospace parts.

The presence of dissolved hydrogen in the melt may be detrimental to the physical and mechanical properties of the aluminum castings due to the porosity associated with this gas.[1] To remove the gas from liquid aluminum, inert gas injection into the aluminum melt through a rotating impeller-injector is the most efficient technology, one which has been employed in industry for decades.[2] This degassing technique reduces hydrogen concentrations to levels below 0.05 mL H/100 g of Al (0.12 wt pct H).[3] Employment of the impeller in the refining of aluminum has the main objective of promoting good stirring in order to improve mixing, which helps to increase the kinetics of gas, impurity and inclusion removal.

Sieverts,[4] Ransley and Neufeld,[5] and Opie and Grand[6] set the base to understand the phenomena occurring during degassing of aluminum based on thermodynamics and the transport phenomena. Due to the opacity of aluminum and the aggressive conditions of temperature during the degassing operation, mathematical and water physical models represent useful tools to understand, control, optimize, and redesign the process. The first mathematical models developed to calculate the rate of hydrogen removal from liquid aluminum melts were based on global mass balances of hydrogen that include the degasification kinetics by defining a global mass transfer coefficient, and as a result of this balance, an ordinary differential equation is derived representing the change of hydrogen concentration in the melt with time.[7,8]

At the end of the twentieth century, numerical simulations of fluid flow in stirred ladles were made considering steady state conditions, and the momentum transfer from the impeller was considered as a special, experimentally determined boundary condition. Maniruzzaman and Makhlouf[9,10] developed a pioneering two-phase mathematical model of aluminum ladles equipped with a

EUDOXIO RAMOS GÓMEZ, formerly Graduate Student with the Metallurgical Engineering Department, Facultad de Química, UNAM, Edificio "D", Circuito de los Institutos s/n, Cd. Universitaria, C.P. 04510 Mexico, DF, Mexico, is now Numerical Simulation Consultant with Cavendish, Mexico, DF, Mexico. ROBERTO ZENIT, Researcher, is with the Materials Research Institute, UNAM, Cd. Universitaria, C.P. 04510 Mexico, DF, Mexico. CARLOS GONZÁLEZ RIVERA and MARCO A. RAMÍREZ-ARGÁEZ, Professors, are with the Metallurgical Engineering Department, Facultad de Química, UNAM. Contact e-mail: marco.ramirez@unam.mx GERARDO TRÁPAGA, Professor, is with the Centro de Investigación y de Estudios Avanzados del IPN, Unidad Querétaro, Libramiento Norponiente 2000, Fracc. Real de Juriquilla, C.P. 76230 Juriquilla, Queretaro, Mexico.

rotating impeller-injector (using the numerical algorithm known as "Volume Of Fluid," VOF, to describe the free surface shape through the commercial code FLUENT v4.4) to predict flow patterns, distribution of bubbles, inclusion trajectories, and turbulence structure for ladles with conventional equipment or REVROT (reverse rotation) equipment. However, it must mentioned that the predicted velocity patterns do not show the expected double circulation loops in the flow patterns for this kind of system. Dong et al.[11] developed a numerical model employing FLUENT v2.97, which predicts 3D flow characteristics of a ladle using the k-ε turbulence model coupled to the Navier–Stokes and continuity equations. Their model assumed the impeller as a stationary plate immersed in a rotary tank. The model was validated with velocity and turbulent kinetic energy experimentally determined in a physical model. Lane et al.[12] developed a mathematical model using a CFD code to predict gas–liquid mixing in a tank equipped with an impeller-injector and a baffle. The calculation was made in 3D, and bubble sizes were varied to account for coalescence and disintegration of bubbles. The zone near the impeller was treated using the Multiple Reference Frame technique, which divides the whole domain into two subdomains, each with its own frame of reference (one is the shaft and the impeller and is set in a rotating frame of reference, while the other is the bath which remains under a stationary frame of reference).[10,13–16] Gas and liquid phases were modeled on a Eulerian frame of reference, and turbulence was accounted for by the standard k-ε model. They obtained liquid velocity patterns, which were found to be qualitatively in good agreement with experimental results. Warke et al.[13] developed a mathematical model to simulate fluid flow phenomena, and gas bubble distribution in a degassing system in order to simulate hydrogen and particle removal from the melt.[14] They validated their results of hydrogen removal with experimental measurements. However, their fluid dynamics calculations present physical inconsistencies at the free surface (liquid velocity vectors leaving the domain) and below the impeller, i.e., continuity does not seem to be satisfied. Fjedl et al.[17] developed a Eulerian 3D mathematical model using FLUENT for the Alcoa A622 degassing unit with 250,000 nodes using the Multiple Reference Frame technique. They were able to determine the bubble size distribution with their model. They also validated their results against experimental kinetics of elimination of Mg from Al by CO_2 injection. Previously, these authors developed a Eulerian–Lagrangian approach using a discrete phase model also cast in FLUENT.[18] Both models present similar results.

Several new features that some studies have included in their models are the coalescence or disintegration of bubbles with bubble size distributions as a process parameter[12] and the presence of inclusions in the melt.[19] Attempts to describe the free surface in aluminum degassing units are also available.[10] Finally, to describe the rotation of the system, different analyses have been employed using a Sliding Mesh technique, where the mesh gradually rotates recalculating the flow field every time step,[20] and using the Multiple Reference

Frame technique. Commonly reported results from mathematical models show contours of gas holdup and bubble size distributions, liquid velocity vector plots, and contour maps of turbulent kinetic energy and its dissipation rate. It is clear that the number and the quality of the mathematical models based on first principles developed so far to describe the cleaning process in ladles equipped with the impeller-injector system are not enough. Besides, some of the above-referenced models do not describe realistically all operations and phenomena occurring during the cleaning step of the process and some of them have not been validated.

In this work, a Eulerian two-phase model was developed to simulate fluid flow and turbulence intensity in a physical model of an aluminum degassing unit employing the impeller-injector technique. The model helped to quantify the degree of stirring produced by gas injection and impeller rotation by varying process parameters such as angular velocity of the impeller, gas flow rate, and the point of gas injection (conventional gas injection through the impeller is compared with novel gas injection from the bottom of the ladle, a technique proposed in this work). The model was reasonably well validated against experimental results obtained in a physical model in terms of flow patterns and shape and size of the vortex.

II. MATHEMATICAL MODELING

The model was based on a full-scale water physical model (constructed specifically for this investigation) of an aluminum batch ladle equipped with an impeller-injector that rotates at high angular velocities (200 to 800 rpm) and that breaks the gas jet, forming small bubbles (3 to 6 mm diameter) and disperses them all over the ladle. In this work, a novel technique of gas injection is proposed that introduces gas through the bottom of the ladle. The angular stirring promoted by the impeller rotation generates a vortex at the free surface of the melt. Figure 1 shows a schematic view of the essential parts of the degasification system (conventional and novel). The process variables considered in this work are rotating speed of the impeller, gas flow rate, and the point of gas injection.

A. Generalities and Assumptions

A two-phase Eulerian–Eulerian mathematical model was developed based on the conservation equations of mass and momentum that govern the turbulent two-phase fluid flow phenomena present in the physical model of the refining aluminum ladle. Governing equations were simultaneously and numerically solved for both phases to simulate and predict fluid flow patterns and turbulent structure in the ladle.

The following assumptions are stated to simplify the problem: (1) constant physical properties of water and air; (2) bubbles are represented by rigid spheres of constant size through the entire volume of the reactor (a bubble diameter of 5 mm was selected since this size was found to represent an average bubble size for most of
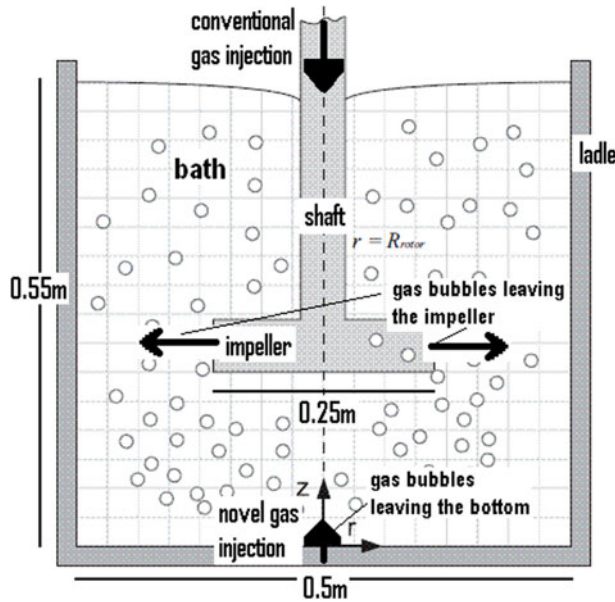
Fig. 1—Schematic of the ladle modeled in this work showing the variables of the process (point of injection, gas flow rate, and rotor speed) and ladle dimensions.

the cases tested in our physical model), *i.e.*, coalescence or disintegration of bubbles is neglected. Additionally, expansion of the bubble is negligible (around 5 pct volume expansion from the bottom to the free surface assuming a static bath and ideal gas in a 0.55-m water column, *i.e.*, bubble size is 5 mm at the bottom and 5.082 mm at the free surface); (3) isothermal bath of Newtonian and incompressible fluid; (4) turbulence represented by the standard *k–ε* turbulence model in 3D. This model is only applied to the liquid phase; (5) an interfacial friction coefficient is employed to describe the drag force exerted by the ascending gas bubbles in the liquid; (6) periodic conditions are set at an angular position of $\pi/4$; and (7) universal wall functions were used to simulate the transitional flow regime from the turbulent core in the melt to the non-slip condition at the static walls.[21]

B. *Governing Equations*

Transport equations governing the fluid dynamics and mass transfer in the degassing ladle are therefore needed to solve this problem based on the two-phase Eulerian–Eulerian approach using the Interpenetrating Slip Algorithm (IPSA), which simulates two-phase flows where one of the phases is dispersed in a second and continuous phase.[22] The governing equations are

(a) Continuity equation for each phase (gas and liquid),

$$\frac{\partial(R_i\rho_i)}{\partial t} + \nabla \cdot (R_i\rho_i u_i) - \nabla \cdot (\rho_i \Gamma_{R_i} \nabla R_i) = 0 \quad [1]$$

where R_i is the volume fraction, ρ_i is the density [kg/m^3], u_i is the velocity vector [m/s], Γ_{R_i} is the phase diffusion coefficient [m^2/s], t is the time [s], and i indicates either water ($i = l$) or gas phase ($i = g$). In Eq. [1], the last

term is an unusual term in the continuity equation, but in multiphase fluid flows, it is an indispensable term through which dispersion of gas in the liquid and the formation of the gas plume may be explained.

The sum of volume fractions of both phases must be equal to one in every location of the domain,

$$R_l + R_g = 1 \quad [2]$$

(b) Momentum conservation equation for both phases (gas and liquid),

$$\frac{\partial(R_i\rho_i u_i)}{\partial t} + \nabla \cdot (R_i\rho_i u_i u_i) - \nabla \cdot (R_i\mu_{\text{eff}}\nabla u_i)$$
$$- \nabla \cdot (u_i\Gamma_{R_i}\nabla R_i) = R_i\nabla P_i + R_i\rho_i\bar{g} + F_{\text{fricc}} \quad [3]$$

where P_i is the pressure of phase i [Pa], g is the gravitational constant [9.81 m/s^2], and F_{fricc} is the momentum exchange between gas and liquid [N/m^3]. Equation [3] has the following terms from left to right: the transient term, the convective transport of momentum, the term of viscous momentum transport within the phase and between the phases, the pressure gradient, body forces (buoyancy) that make the bubbles ascend through the melt since the gas phase is less dense than liquid metal, and the friction forces or momentum exchange between the phases. This last term plays an important role in the calculation since the drag force that gas exerts on the liquid (or *vice versa*) promotes stirring in the bath. This force term has the same magnitude for the gas and liquid phases in the momentum conservation equations, but different signs:

$$F_{\text{fricc}} = C_f(u_i - u_j) \quad [4]$$

where C_f is the friction coefficient involving the drag coefficient, C_D, which in turn was taken from an empirical correlation.[22] Turbulent Reynolds stresses were treated by the Bussinesq approach.[23] μ_{eff} is the effective viscosity [kg/ms], which is the sum of the molecular viscosity (μ) and the turbulent viscosity [kg/ms]:

$$\mu_{\text{eff}} = \mu + \mu_t \quad [5]$$

(c) Conservation equations for the turbulent kinetic energy (k) and its dissipation rate (ε) involved in the *k–ε* turbulence model of Launder and Spalding[24] (only applied to the liquid phase),

$$\frac{\partial(\rho_l k)}{\partial t} + \nabla \cdot (\rho_l u_l k) = \nabla \cdot \left(\frac{u_{\text{eff}}}{\sigma k}\nabla k\right) + R_l\rho_l(G - \varepsilon) \quad [6]$$

$$\frac{\partial(\rho_l \varepsilon)}{\partial t} + \nabla \cdot (\rho_l u_l \varepsilon) = \nabla \cdot \left(\frac{u_{\text{eff}}}{\sigma_K}\nabla\varepsilon\right) + R_l\rho_l\frac{\varepsilon}{k}(C_1 G - C_2\varepsilon)$$
$$[7]$$

where G is the generation of turbulent kinetic energy and the turbulent viscosity (μ_t) [kg/ms] is computed with the standard *k–ε* model as
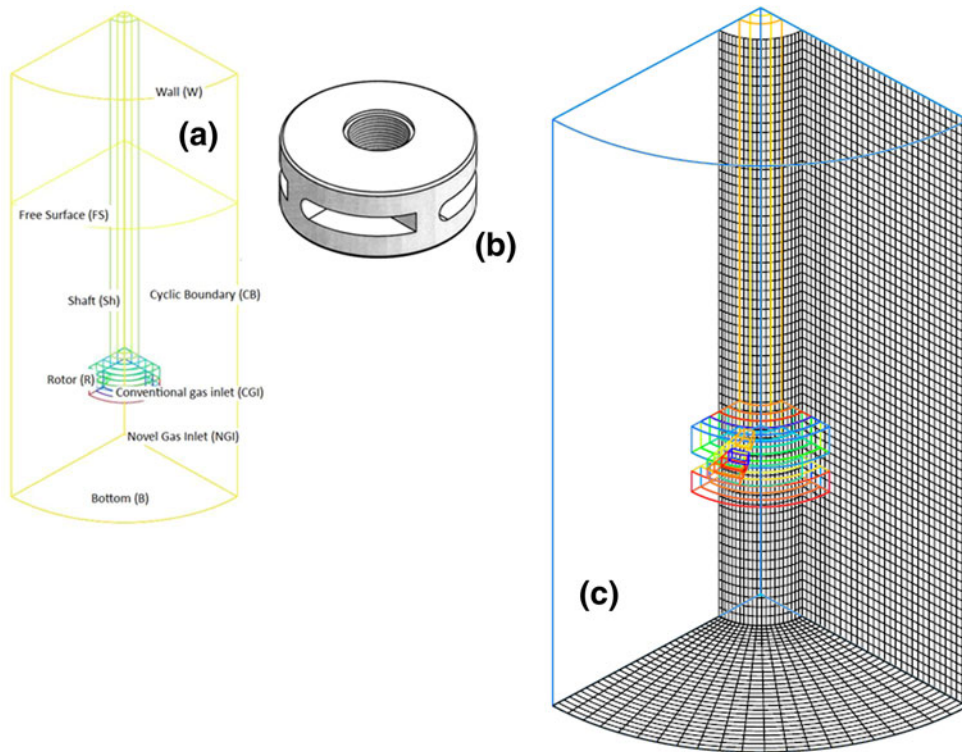
Fig. 2—(a) Boundaries of the system, (b) impeller geometry, and (c) grid used.

Table I. Boundary Conditions Used in This Work (Subscripts of Velocities are r, θ, and z to Represent Each Velocity Component in Cylindrical Polar Coordinates)

Variable	Sh	R	W	B	CGI	NGI	FS	CB
$u_{\theta,l}$	u_{shaft}	u_{rotor}	0	0	0	0	$\frac{\partial u_{\theta,l}}{\partial Z}=0$	$\frac{\partial u_{\theta,l}}{\partial \theta}=0$
$u_{\theta,g}$	u_{shaft}	u_{rotor}	0	0	0	0	$\frac{\partial u_{\theta,g}}{\partial z}=0$	$\frac{\partial u_{\theta,g}}{\partial \theta}=0$
$u_{r,l}$	0	0	0	0	0	0	$\frac{\partial u_{r,l}}{\partial z}=0$	$\frac{\partial u_{r,l}}{\partial \theta}=0$
$u_{r,g}$	0	0	0	0	0	0	$\frac{\partial u_{r,g}}{\partial z}=0$	$\frac{\partial u_{r,g}}{\partial z}=0$
$u_{z,l}$	0	0	0	0	0	0	0	$\frac{\partial u_{z,l}}{\partial \theta}=0$
$u_{z,g}$	0	0	0	0	inlet velocity	inlet velocity	$\frac{\partial u_{z,g}}{\partial z}=0$	$\frac{\partial u_{z,g}}{\partial \theta}=0$
k	wall function	wall function	wall function	wall function	k_{inlet}	k_{inlet}	$\frac{\partial k}{\partial z}=0$	$\frac{\partial k}{\partial \theta}=0$
ε	0	0	wall function	wall function	ε_{inlet}	ε_{inlet}	$\frac{\partial \varepsilon}{\partial z}=0$	$\frac{\partial \varepsilon}{\partial \theta}=0$
R_l	$\frac{\partial R_l}{\partial r}=0$	$\frac{\partial R_l}{\partial r}=0$	$\frac{\partial R_l}{\partial r}=0$	$\frac{\partial R_l}{\partial r}=0$	0	0	0	$\frac{\partial R_l}{\partial \theta}=0$
R_g	$\frac{\partial R_g}{\partial r}=0$	$\frac{\partial R_g}{\partial r}=0$	$\frac{\partial R_g}{\partial r}=0$	$\frac{\partial R_g}{\partial r}=0$	1	1	1	$\frac{\partial R_g}{\partial \theta}=0$

Table II. Physical Properties of Air and Water[25]

Property	Viscosity, μ (kg/m s)	Density, ρ (kg/m^3)	Kinematic Viscosity, v (m^2/s)
Water	1×10^{-3}	1000	1×10^{-6}
Air	1.383×10^{-5}	1.23	1.124×10^{-5}

$$\mu_t = \frac{\rho_l c_\mu k^2}{\varepsilon} \qquad [8]$$

Values of the constants C_1, C_2, C_μ, σ_k, and σ_ε are 1.44, 1.92, 0.09, 1.0, and 1.314, respectively.[24]

C. Boundary and Initial Conditions

Figure 2(a) shows a scheme where all boundaries of the ladle equipped with the impeller can be appreciated in a cylindrical coordinate system in 3D. In this figure, region FS represents the free surface above which air is present,
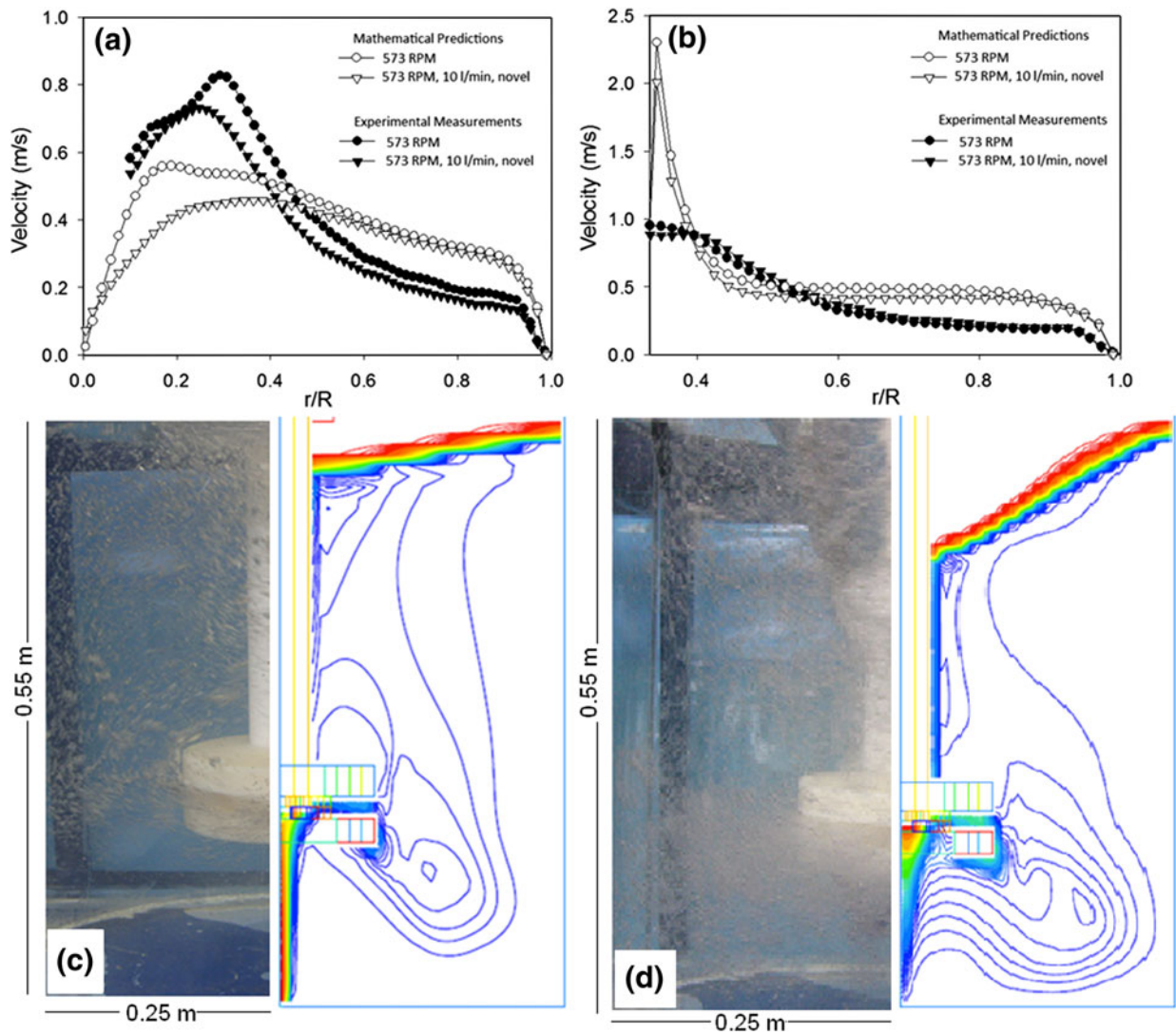
Fig. 3—Mathematically predicted and experimental radial liquid velocity profiles: (*a*) at 9 cm and (*b*) at 18 cm from the bottom of the ladle, both at 573 rpm, without gas injection and with (10 L/min). Comparison of predicted vortex size and gas hold with observations from a water physical model with parameters: (*c*) 290 rpm and 10 L/min novel gas injection and (*d*) 573 rpm and 10 L/min, novel gas injection.

since the interface between the liquid and the atmosphere lay inside the computation domain. Region W represents the lateral walls. Region B represents the bottom of the ladle. Regions CGI and NGI represent the gas inlet for the conventional and novel point of gas injection (the impeller used in this simulation has four nozzles), and finally region CB represents cyclic boundary conditions meaning that velocities and other features will have cyclic patterns and values in the rest of the ladle. Since the impeller has four nozzles separated by the same distance, we only considered ¼ of the ladle as a computational domain in order to minimize the size of the grid and calculation time. At the static walls, non-slip conditions and the use of universal wall functions were used to compute the low Reynolds number flow regime near the static wall from the turbulent region in the rest of the ladle, while at the moving walls (region R and Sh for impeller and shaft surfaces), the non-slip condition is also applied. At the free surface, there are no viscous stresses and the gas injected through the impeller escapes to the

atmosphere at this free surface. Finally, at the nozzle, gas enters at given axial and angular velocities as actually happens in the real process. Table I shows explicitly all boundary conditions. Initial conditions represent a static fluid with a ladle filled with water and the rest of the domain above the liquid is atmospheric gas.

D. *Physical Properties*

Values of physical and transport properties of water and air are shown in Table II, while the ladle and impeller dimensions are presented in Figure 1.

E. *Solution*

The system of partial differential equations that governs the operation of these reactors, subjected to their respective boundary conditions, is solved simultaneously and numerically using the commercial computational fluid dynamics (CFD) code PHOENICS version
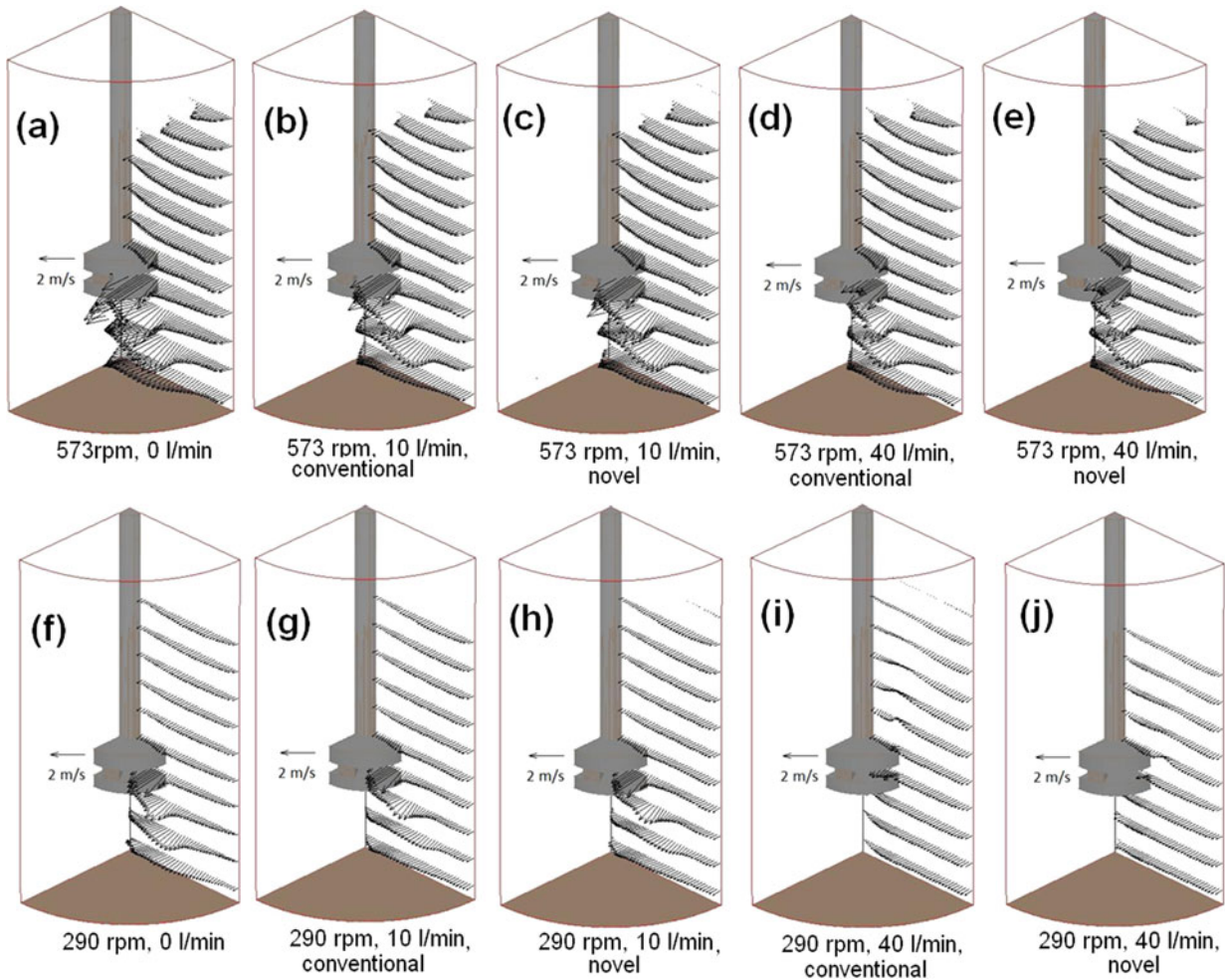
Fig. 4—Velocity vector maps of liquid plotted at different transverse planes, showing developed flow patterns.

3.4, using the IPSA algorithm. In order to minimize the numerical diffusion at the liquid free surface, the higher-order convective numerical scheme Superbee[22] was used for all variables. Each simulation took approximately 73.5 hours of computation time to solve the problem (using a PC with a 2GHz Intel® processor with 1 GB RAM) so that steady conditions were reached in the cylindrical mesh. This grid, selected after a sensitivity analysis to optimize computer time without losing significant precision in the calculation, is an orthogonal cylindrical grid with 52,920 cells (see Figure 1(c)) maintaining an aspect ratio close to one ($\Delta z/\Delta r \sim 1$) to improve convergence of simulations and a value of the mesh size in the radial and axial directions of approximately 0.33 cm.[26] Variables explored in this work were (1) impeller speed (290 and 573 rpm), (2) gas flow rate (0, 10, and 40 L/min), and (3) point of gas injection into the bath, *i.e.*, conventional (through the impeller) and novel (through the ladle bottom). The design of the impeller, a commercial design by FOSECO®, is shown in Figure 2(b). The impeller's middle line is always located at a depth of 18 cm from the bottom of the vessel.

III. RESULTS AND DISCUSSION

A. *Validation of the Mathematical Model*

One of the major drawbacks of the previous models is the lack of rigorous validation against experimental results. The current mathematical model was validated by comparing the experimental measurements of velocity obtained by Particle Image Velocimetry (PIV) in a physical model[26] with predictions from this model. Figure 3 presents computed and measured liquid velocity magnitude radial profiles at heights of 9 cm (Figure 3(a)) and 18 cm (Figure 3(b)) from the bottom of the ladle. Comparisons at planes above the impeller level were incomplete because the impeller visually blocked the camera. Two gas conditions were included (0 and 10 L/min), with the gas injected in the novel way through the bottom of the ladle, and with an angular impeller speed of 573 rpm.

Both magnitude and trend show reasonably good agreement between experiments and simulations. At the plane located at 9 cm from bottom, simulations over-estimate velocities near the wall ($r/R = 1$), but under-estimate them near the impeller ($r/R = 0$), while at the
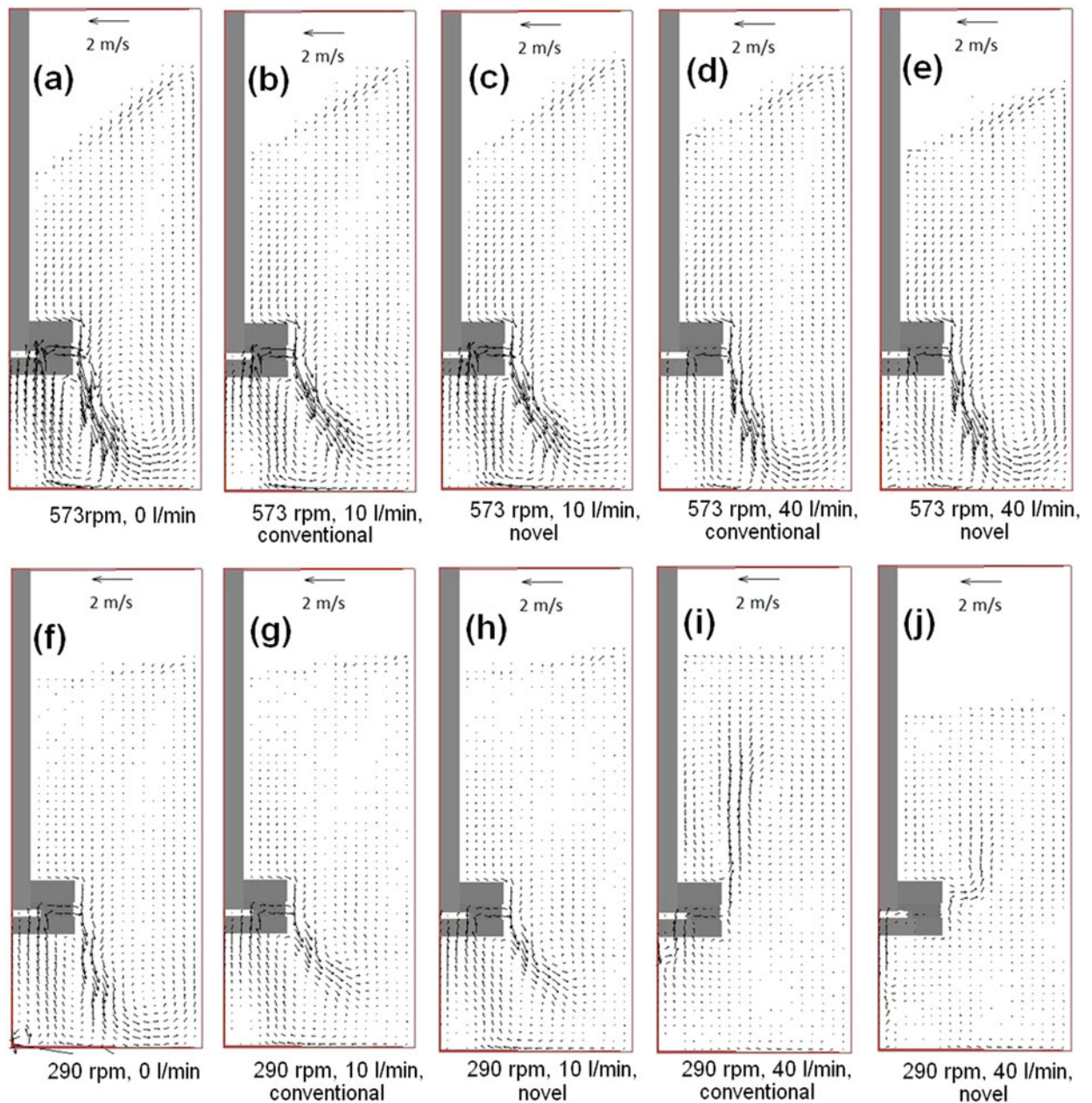
Fig. 5—Velocity vector maps of liquid plotted along a longitudinal plane, showing developed flow patterns.

plane at 18 cm from bottom, simulations slightly over-estimate velocities near the wall and significantly over-estimate them near the symmetry axis (impeller). Despite these differences and considering the complexity of the problem, agreement is reasonably good in the trend between experiments and simulations. Figures 3(c) and (d) show a qualitative comparison of predicted and observed vortex sizes and gas holdup for 573 rpm, 10 L/min novel injection and 290 rpm, 10 L/min novel injection, respectively. Again, some differences are observed between experiments and predictions, but the trend shows agreement in both vortex size and gas holdup for these two cases.

B. Liquid Velocity Fields

Figure 4 shows the liquid velocity fields plotted at 11 transversal planes (r–θ planes) under all the operational conditions of rotor speed, gas flow rate, and point of injection explored in this work. From these plots, the 3D nature of the flow field patterns developed during the stirring of the liquid by the impeller and by the gas injection is clear, but the flow is preferentially directed in the angular axis, which indicates that stirring is governed by momentum transfer from the impeller to the liquid. This is why higher velocities are calculated closer to the impeller.

Figure 5 shows the same cases as in Figure 4, but in this case, liquid velocity fields are plotted in longitudinal
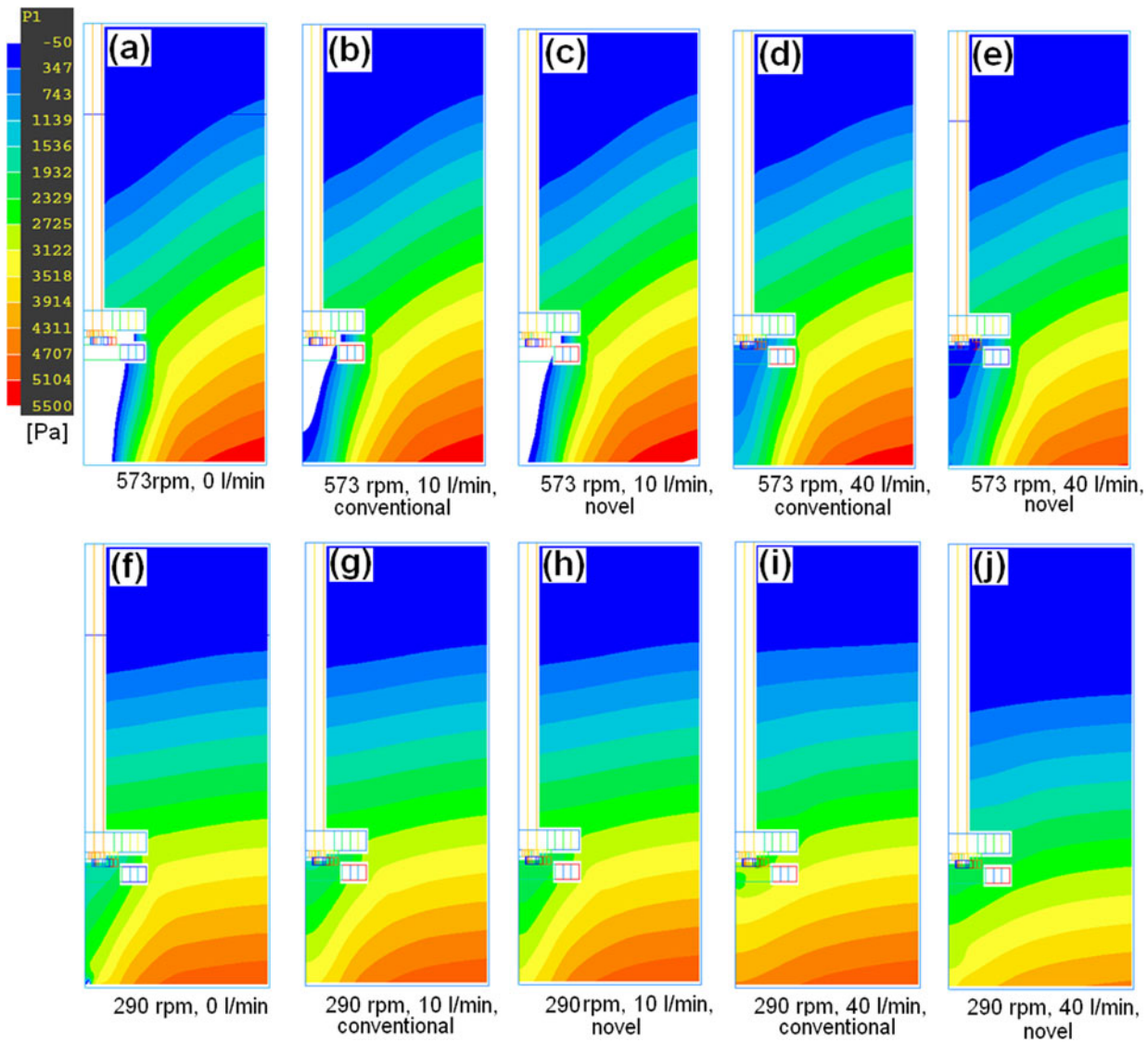
Fig. 6—Pressure contours in [Pa] of the liquid plotted along a longitudinal plane, showing developed flow patterns.

planes such that the angular motion of the liquid is not seen, but where axial and radial components of velocities are clearly observed. This view shows the size of the vortex formed as a consequence of the balance of radial forces, where centrifugal forces and pressure gradients are mainly controlled by the speed of the impeller (the greater the speed, the greater the vortex size) and to a lesser degree by the gas flow rate (the greater the gas flow, the lower the vortex size). The well-known pumping effect of the impeller is seen from the same figure. Rotation of the impeller and its bottom hole geometry results in a pressure drop below the impeller that draws fluid from the surroundings, and the fluid is expelled from the impeller nozzles toward the lateral walls of the ladle with a discharge angle of 45 deg horizontal. The pumping effect is claimed to increase stirring in the melt and to accelerate removal kinetics[27] and this is the reason why this effect may be properly designed from the geometry of the impeller using CFD

techniques. The pumping effect is greater with the higher impeller rotation speed, with a low gas injection rate, and with the novel gas injection from the bottom of the ladle. This pumping effect of the impeller dominates the flow pattern in this plane. Two circulation loops are observed. A clockwise loop is located below the impeller, and above the discharge of fluid, there is a counterclockwise loop. When the rotation speed is low (290 rpm) and the gas flow rate is high (40 L/min), those circulations disappear and the fluid dynamics of the liquid is governed by the gas ascending through the liquid due to drag forces rather than momentum transfer from the impeller to liquid, which was confirmed by the results obtained from the physical model.[26] At high rotation speeds, gas injection from the bottom improves the pumping effect of the impeller relative to the conventional gas injection, but at low rotor speeds, both injection methods perform similarly.
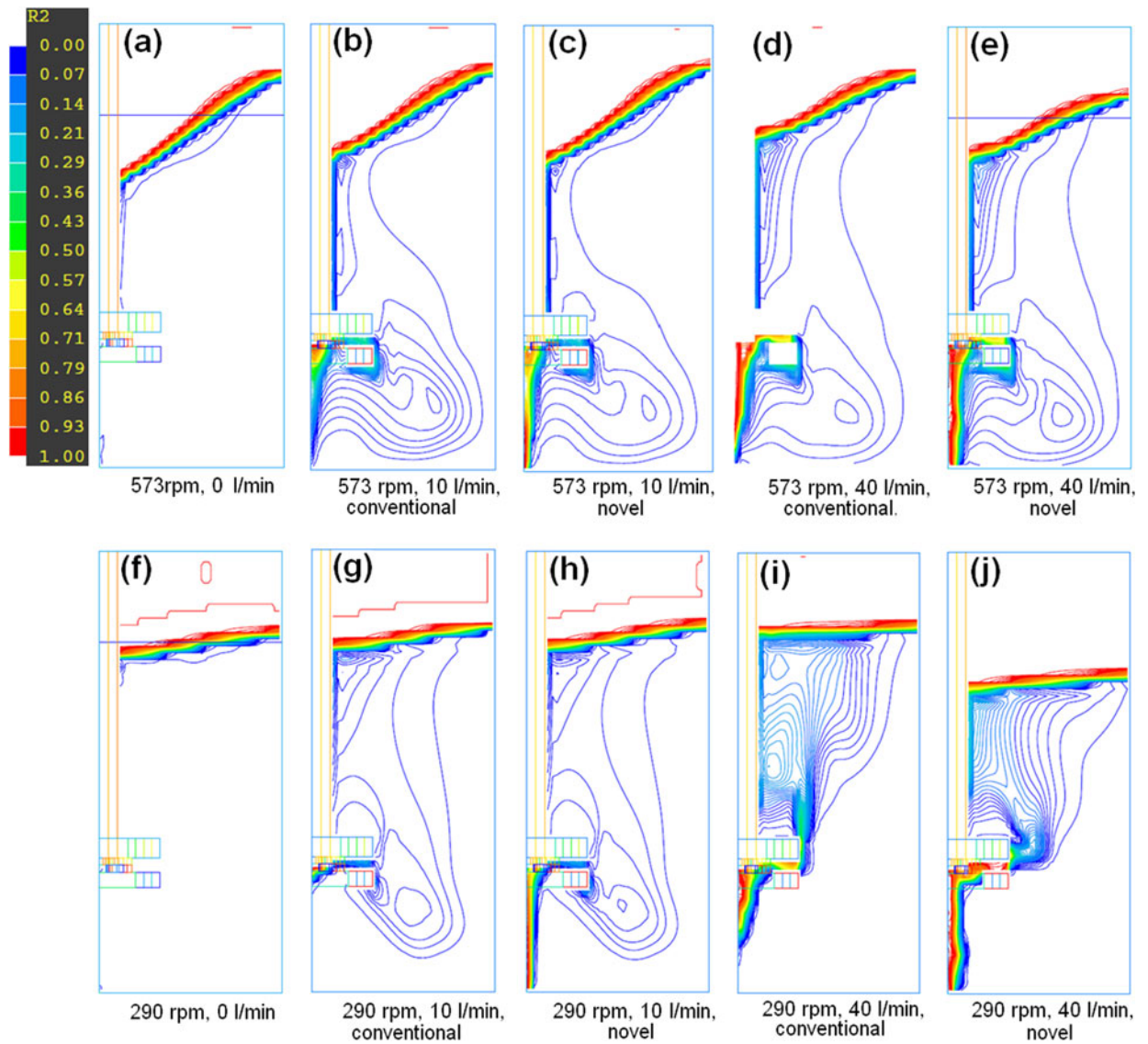
Fig. 7—Gas holdup contours along a longitudinal plane, showing developed flow patterns.

C. *Pressure Contours*

Pressure contours are presented in Figure 6 for all cases considered in this work. In the static state of the bath (no rotation of impeller), horizontally flat pressure profiles would be seen corresponding to differences in hydrostatic pressure. When the impeller rotates, centrifugal forces push liquid toward the ladle wall in a radial direction and this force has to be balanced by a pressure gradient to reach mechanical equilibrium. Thus, centrifugal forces are responsible for the presence of radial pressure gradients close to the impeller and the entire pressure profile inside the ladle generates the vortex shape and size. Figure 6 demonstrates that the centrifugal forces and vortex size increase when the rotation speed of the impeller increases and when gas flow rate decreases. The pressure drop below the impeller is the factor that creates the pumping effect of the impeller, which is magnified at high rotation speeds and by the

novel injection of gases. In a previous study,[22] it was concluded that gas injection is detrimental for the stirring of the liquid because of a zone of gas (formed by the bubbles) that surrounds the impeller, impeding the momentum transfer from the impeller to the liquid. The novel injection seems to improve momentum transfer from the impeller, producing a more agitated bath than conventional injection gases techniques through the impeller's nozzles.

D. *Gas Holdup Contours*

Gas holdup contours are presented in Figure 7 for all cases and conditions reported. These contours illustrate gas bubble dispersion through the melt and the size and shape of the vortex. Despite the coarse grid used in the simulations, numerical diffusion at the free surface is not an issue in these calculations as the vortex size is
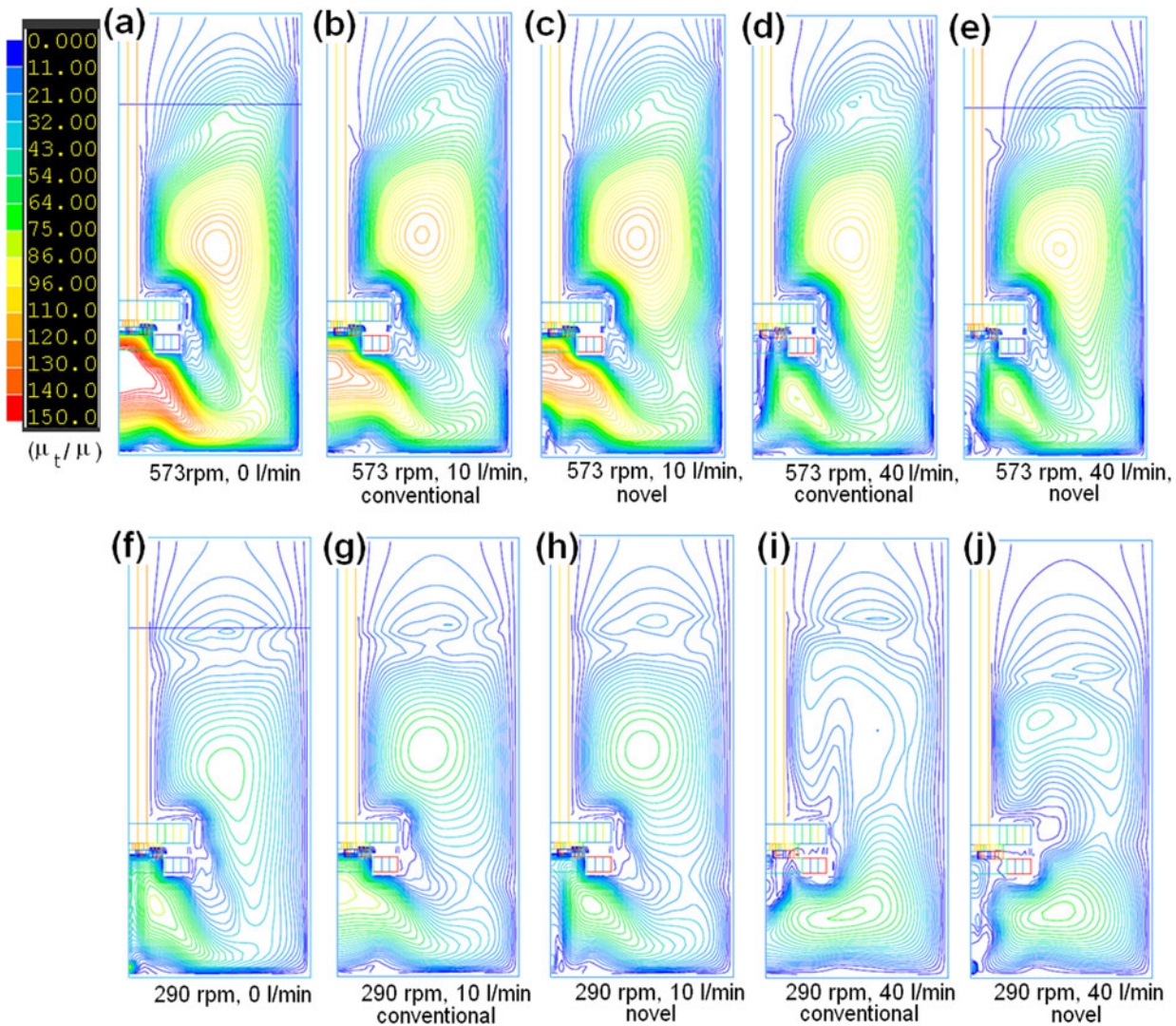
Fig. 8—Viscosity ratio (μ_t/μ) contours along a longitudinal plane, showing developed flow patterns.

relatively sharp and clearly defined. The results show large vortices formed at high impeller speed conditions and a strong dispersion of bubbles below the impeller regardless the gas flow rate or point of gas injection. On the contrary, when the impeller operates at low rotation speeds, dispersion of bubbles is poor and vortex size decreases. Interestingly, when the gas flow rate is high (40 L/min) and the impeller speed remains low (290 rpm), the gas plume presents the worst dispersion, and the plume concentrates near the shaft and near the impeller, which would suggest bad stirring conditions for the ladle, likely resulting in slow impurity removal rates. The model results do not resolve differences in the gas zone covering the impeller obtained with novel and conventional injections. However, it is known that this gas zone inhibits momentum transfer from the impeller to the liquid when gas is injected conventionally through the rotor's nozzles.[28]

E. Turbulent Kinematic Viscosity Contours

Turbulent kinematic viscosity (μ_t/ρ) represents the degree of turbulence in the system. Figure 8 presents maps of the ratio between turbulent kinematic viscosity and molecular kinematic viscosity for all cases and conditions explored in this work. Two zones of high turbulence are found, one is below the impeller and the other is above and to the right. Turbulence below the impeller decreases as the gas flow rate increases, but the injection point of gas seems to have no effect on the turbulence's intensity.

It is clear that the impeller speed is the variable that controls most the degree of turbulence in the ladle. The greater the impeller rotation speed, the more turbulent the flow. Turbulence is beneficial to increase mass and momentum transfer rates, which may increase the rate of gas and impurity removal. Turbulence also promotes homogeneity of gas concentration and temperature in the system. Gas flow rates and point of injection do not
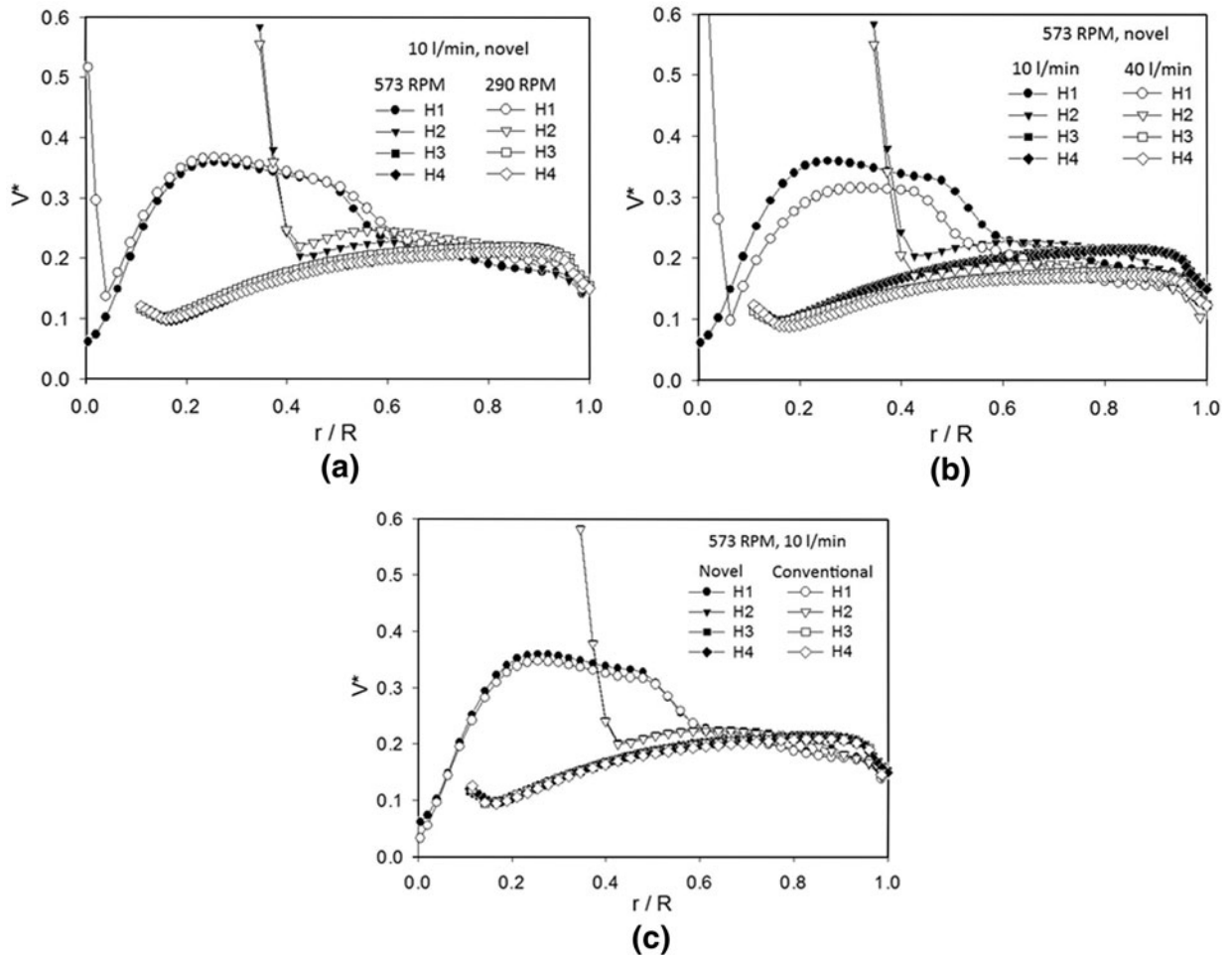
Fig. 9—Velocity magnitude at different heights from the ladle bottom (H1 = 9 cm, H2 = 18 cm, H3 = 30 cm, and H4 = 39 cm) and exploring the influence of different process conditions: (*a*) effect of impeller speed, (*b*) effect of gas flow rate, and (*c*) effect of gas injection point.

influence the turbulence in the ladle at the same level as the rotor speed does.

F. Velocity and Turbulent Radial Profiles

Figures 9 and 10 present radial profiles of dimensionless liquid velocities (obtained by dividing the liquid velocity by the velocity of the external radius of the impeller) and dimensionless turbulence intensities, respectively. These profiles are presented at different heights from the bottom of the ladle (H1 = 9 cm, H2 = 18 cm, H3 = 30 cm, and H4 = 39 cm, for reference, the impeller depth is 18 cm). When velocity is plotted in the dimensionless form, as it is in Figure 9, the radial velocity profiles at both impeller speeds are identical (Figure 9(a)), suggesting the same turbulent flow regime at both speeds and also that the liquid velocity magnitude is linearly proportional to the impeller speed. The curves in Figure 9(c), where the

gas injection points are compared, are nearly identical to those of Figure 9(a), where the impeller speeds are compared. In the case of Figure 9(c), the novel gas injection technique shows slightly higher velocities than the conventional technique. In contrast to the limited effects of impeller speed and gas injection point, increasing the gas flow rate significantly decreases the dimensionless velocity (Figure 9(b)). This means that the gas flow rate inhibits the stirring effect of the impeller due to the inefficient momentum transfer from the impeller due to the gas zone created between the impeller and the liquid.

Figure 10 presents the effects of impeller speed (Figure 10(a)), gas flow rate (Figure 10(b)), and type of gas injection (Figure 10(c)) on the turbulence intensity of the liquid. Higher gas flow rate, lower impeller rotation speed, and using the conventional gas injection technique decrease turbulence intensity in the ladle.
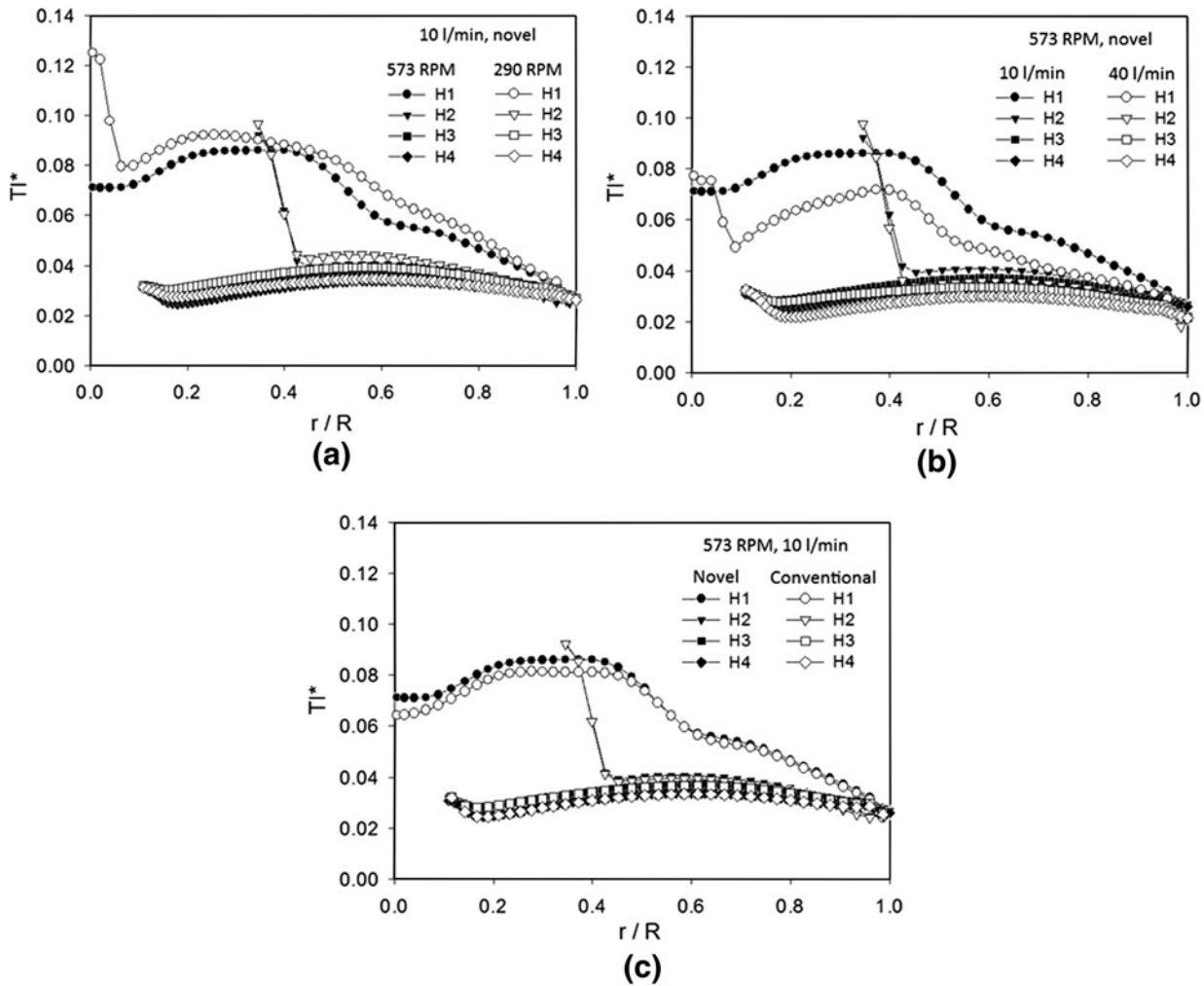
Fig. 10—Turbulent intensity radial profiles at different heights from ladle bottom (H1 = 9 cm, H2 = 18 cm, H3 = 30 cm, and H4 = 39 cm) and exploring the influence of different process conditions: (a) effect of impeller speed, (b) effect of gas flow rate, and (c) effect of gas injection point.

IV. CONCLUSIONS

In this work, we conducted a 3D numerical simulations using a Euler–Euler-based model implemented into the commercial CFD code PHOENICS 3.4.

The model was validated by comparing liquid velocity radial profiles predicted with this model against measurements obtained by PIV in a water physical model built by the same research group. Validation was reasonably good in trend, but some marked quantitative differences were found between simulated and measured results. Vortex sizes predicted by the model were also qualitatively compared with experimental observations showing reasonably good agreement.

Simulations show the flow structure of a physical model of an aluminum ladle for degassing with an injector-rotating impeller. The flow is 3D in nature, but the angular component of the velocity dominates the motion of the liquid due to the momentum exchange between the impeller and the bath. Only at high gas flow rates (40 L/min) and low impeller rotating speeds (290 rpm) is liquid motion dominated by the drag

between the liquid and bubbles ascending vertically through the ladle.

Impeller stirring performance is related to the pumping effect, which is due to the pressure drop below the impeller that sucks fluid from the bottom of the impeller and ejects it toward the ladle walls in a radial direction. The pumping effect is increased by increasing the rotating speed and by injecting gas from bottom of the ladle, but decreases as the gas flow rate increases.

As the speed of the impeller increases, stirring of the bath increases proportionally (improving momentum transfer from the impeller to the bath), velocity and turbulence in the system are increased, bubble dispersion is better, and the pumping effect of the impeller is magnified (probably good conditions for cleaning purposes), but the vortex size also increases, which may be detrimental.

As the gas flow rate increases, stirring of the liquid decreases, the pumping effect of the impeller is diminished, and bubble dispersion decreases (probably detrimental conditions for cleaning), while vortex size decreases. The

gas leaving the impeller forms a gap (gas zone) adjacent to the impeller that prevents momentum exchange.

Finally, the injection point is the least significant variable in the agitation of the bath, but at high impeller speeds, the novel injection point from the bottom of the ladle slightly improves agitation compared to the conventional gas injection through the impeller. This novel gas injection may represent a cost-effective option in the refining of aluminum, avoiding the more complex injection of gas through the shaft and impeller, components that are frequently replaced when cracks are observed. These components would last longer (even if they have cracks) in the novel injection proposed in this work, since gases do not flow through them.

ACKNOWLEDGMENTS

REFERENCES

1. Q.T. Fang and D.A. Gragner: *AFS Trans.*, 1989, vol. 97, pp. 989–1000.
2. G.K. Sigworth: *Mod. Cast.*, 1988, vol. 3, pp. 42–44.
3. M. Makhlouf: *Report on Measurement and Removal of Hydrogen in Aluminum Alloys*, American Foundrymen's Society, Orlando, FL, 1998.
4. A. Sieverts: *Z. Metallkunde*, 1929, vol. 21, pp. 37–46.
5. C.E. Ransley and H. Neufeld: *J. Inst. Met.*, 1947–1948, vol. 74, pp. 559–620.
6. W.R. Opie and W. Grant: *Trans. AIME*, 1950, vol. 188, pp. 1237–41.
7. G.K. Sigworth and T.A. Engh: *Metall. Trans. B*, 1982, vol. 13B, pp. 447–60.
8. J.G. Stevens and H. Yu: *Light Met.*, 1992, vol. 121, pp. 1023–29.
9. M. Maniruzzaman and M. Makhlouf: *Light Met.*, 1997, vol. 127, pp. 797–803.
10. M. Maniruzzaman and M. Makhlouf: *Metall. Mater. Trans. B*, 2002, vol. 33B, pp. 297–303.
11. S.T. Dongs, T. Johansen, and A. Engh: *Chem. Eng. Sci.*, 1994, vol. 49, pp. 3511–18.
12. G.L. Lane, M.P. Schwarz, and G.M. Evans: *Appl. Math. Model.*, 2002, vol. 26, pp. 223–35.
13. V.S. Warke, G. Tryggvason, and M.M. Makhlouf: *J. Mater. Process. Technol.*, 2005, vol. 168, pp. 112–18.
14. V.S. Warke, S. Shankar, and M.M. Makhlouf: *J. Mater. Process. Technol.*, 2005, vol. 168, pp. 119–26.
15. J.L. Song, M.R. Jolly, M. Kimata, W. Bujalski, and A.W. Nienow: *Third International Conference on CFD in the Minerals and Process Industries*, CSIRO, Melbourne, Australia, December 2003.
16. C. Gentric, D. Mignon, J. Bousquet, and P.A. Tanguy: *Chem. Eng. Sci.*, 2005, vol. 60, p. 2253.
17. A Fjeld, SS Edussuriya, JW Evans, and A Mukhopadhyay: *Light Met.*, 2005, vol. 34, pp. 963–68.
18. A. Fjeld, J.W. Evans, and D.C. Chesonis: *Light Met.*, 2006, vol. 35, pp. 771–76.
19. O. Mirgaux, D.A. Blitzer, E. Waz, and J.P. Bellot: *Metall. Mater. Trans. B*, 2009, vol. 40B, pp. 363–75.
20. N.G. Deen, T. Solberg, and B.H. Hjertager: *Can. J. Chem. Eng.*, 2002, vol. 80, pp. 638–52.
21. J. Nikuradse: *Ver. Dsch. Ing. Forsh.*, 1933, vol. 4, pp. 356–61.
22. PHOENICS On-Line Information System (POLIS): PHOENICS 3.4, CHAM Company, London, 2000.
23. J. Szekely: *Fluid Flow Phenomena in Metals Processing*, Academic Press, New York, 1988, p. 43.
24. B.E. Launder and D.B. Spalding: *Comput. Method. Appl. Mech. Eng.*, 1974, vol. 3, pp. 269–89.
25. D. Green and R. Perry: in *Perry's Chemical Engineers' Handbook*, 8th ed., McGraw-Hill, New York, 2007, section 2.
26. E. Ramos-Gomez: M.Sc. Thesis, Universidad Nacional Autónoma de México, Mexico City, 2011.
27. J.Y. Oldshue and N.R. Herbst: in *A Guide to Fluid Mixing*, 3rd ed., Lightning, Rochester, NY, 2003.
28. J.L. Camacho-Martínez, M. A. Ramírez-Argáez, R. Zenit, A. Juárez-Hernández, and O. Barceinas: *Mater. Manuf. Process.*, 2010, vol. 25, pp. 1–11.